Finite Element Analysis of the Mouse Proximal Ulna in Response to Elbow Loading

Feifei Jiang[1], Aydin Jalali[2], Chie Deguchi[2, 3], Andy Chen[2], Shengzhi Liu[2, 4], Rika Kondo[2, 5], Kazumasa Minami[5], Takashi Horiuchi[3], Bai-Yan Li[4], Alexander G. Robling[6], Jie Chen[1], and Hiroki Yokota[1, 2, 4, 6]

[1]Department of Mechanical Engineering, Indiana University Purdue University Indianapolis, Indianapolis, IN 46202, USA
[2]Department of Biomedical Engineering, Indiana University Purdue University Indianapolis, Indianapolis, IN 46202, USA
[3]Graduate School of Engineering, Mie University, Mie 514, Japan
[4]Department of Pharmacology, School of Pharmacy, Harbin Medical University, Harbin 150081, China
[5]Osaka University Graduate School of Medicine, Suita, Osaka 565, Japan
[6]Department of Anatomy and Cell Biology, Indiana University School of Medicine, Indianapolis, IN 46202, USA

Keywords: Finite element analysis, ulna, mechanical loading, strain

Running title: FE analysis in response to elbow loading

Corresponding Author:

Hiroki Yokota, PhD
Department of Biomedical Engineering
Indiana University-Purdue University Indianapolis
723 West Michigan Street, SL220
Indianapolis, IN 46202 USA
Phone: 317-278-5177; Fax: 317-278-2455
Email: hyokota@iupui.edu

This is the author's manuscript of the article published in final edited form as:
Jiang, F., Jalali, A., Deguchi, C., Chen, A., Liu, S., Kondo, R., … Yokota, H. (2018). Finite-element analysis of the mouse proximal ulna in response to elbow loading. Journal of Bone and Mineral Metabolism. https://doi.org/10.1007/s00774-018-0943-y

Abstract

Bone is a mechano-sensitive tissue that alters its structure and properties in response to mechanical loading. We have previously shown that application of lateral dynamic loads to a synovial joint, such as the knee and elbow, suppresses degradation of cartilage and prevent bone loss in arthritis and postmenopausal mouse models, respectively. While loading effects on pathophysiology have been reported, mechanical effects on the loaded joint are not fully understood. Because the direction of joint loading is non-axial, not commonly observed in daily activities, strain distributions in the laterally loaded joint are of great interest. Using elbow loading, we herein characterized mechanical responses in the loaded ulna focusing on the distribution of compressive strain. In response to 1 N peak-to-peak loads, which elevate bone mineral density and bone volume in the proximal ulna *in vivo*, we conducted finite element analysis and evaluated strain magnitude in three loading conditions. The results revealed that strain of ~1,000 μstrain (equivalent to 0.1% compression) or above was observed in the limited region near the loading site, indicating that the minimum effective strain for bone formation is smaller with elbow loading than axial loading. Calcein staining indicated that elbow loading increased bone formation in the regions predicted to undergo higher strain.

Introduction

To prevent bone loss associated with postmenopausal osteoporosis, the benefits of physical activities are well supported by clinical data (1, 2). An important physiological component of physical activity is mechanical loading to the bone matrix, and accumulating evidence supports that bone cells are sensitive to mechanical stimulation (3, 4). As currently understood, the osteocyte, the most abundant cell in bone matrix, acts as a mechano-sensor to activate the development of bone-forming osteoblasts (5, 6). In pre-clinical studies, various loading modalities, such as ulna loading, tibia loading, etc., have been employed, and the loading conditions that elevate bone mass and bone mineral density have been investigated (7-9). Among previous and on-going studies, dynamic strain in bone matrix and strain-induced fluid flow in the lacuno-canalicular network are two of the major contributors to mechanotransduction in bone (10, 11).

Unlike axial loading, such as in ulna and tibia loading, joint loading employs lateral loads that sandwich a synovial joint, such as the knee, ankle, and elbow (12 – 14). Knee loading, for instance, is shown to reduce tissue degeneration by inhibiting the responses to inflammatory cytokines and downregulating matrix metalloproteinases (15, 16). It is also reported that knee loading stimulates bone formation in the lower limbs and promotes fracture healing in the femur (17, 18). Elbow loading, another joint loading modality with lateral loads, is reported to inhibit degeneration of cartilage tissue and promote bone formation (19, 20). While biological characterization in response to joint loading has been investigated, including its effects on ischemic necrosis, angiogenesis, and obesity-related fatty liver disease (21 – 23), its mechanical effect on bone matrix has not been fully analyzed. While joint loading with lateral loads may not

be commonly encountered in daily physical activities, it could potentially offer a novel form of physical therapy in patients with reduced mobility for decreasing inflammatory responses or preventing bone loss in the cartilage and long bones.

In this study, we determined the strain distribution to the ulna in response to elbow loading using a mouse model and finite element (FE) analysis. Daily loading with 1 N peak-to-peak force at 1 Hz for 5 min was applied to ovariectomized (OVX) mice as well as sham-OVX mice (control mice), and bone mineral density (BMD) was measured at the site of loading after 4 weeks of loading. We first examined whether ovariectomy surgery reduces BMD in the proximal ulna, and whether elbow loading elevates BMD locally. After confirming the effective loading condition, we conducted FE analysis of the proximal ulna using the same loading force. Our primary aim was to predict the maximum value of compressive strain in response to elbow loading. We employed three loading configurations: load and a single point of support, load and a three-point support, and load across soft tissues that may mimic surrounding skin and muscle. While no model may precisely represent the true loading conditions *in vivo*, we present a comparative analysis of these configurations to facilitate our overall understanding of the effects of joint loading. The result indicates that the maximum compressive strain is 0.1% (1,000 μstrain) and beyond in the load-adjacent regions in response to elbow loading with 1 N loads.

Materials and Methods

Animal model. The experimental procedure was approved by the Indiana University Animal Care and Use Committee and was in compliance with the Guiding Principles in the Care and Use of Animals endorsed by the American Physiological Society. Forty BALB/c female mice (~12 weeks, Harlan Laboratories, Indianapolis, IN, USA) were employed. They were fed with mouse chow and water *ad libitum*, and divided into four groups: ovariectomized (OVX) mice with and without elbow loading, and sham-OVX mice with and without elbow loading. Ovariectomy was conducted using the procedure previously employed (23), and sham-OVX mice received sham surgery in which the same operation was conducted without removing ovaries. The animals were given 4 weeks after surgery to recover before beginning elbow loading. The animals were sacrificed after 5 weeks of daily loading, and the ulnae were harvested for characterization.

Elbow loading. Elbow loading was conducted using Electro Force 3100 (Bose, Inc., Framingham, MA, USA) using the same procedure previously described (24) (**Fig. 1A & B**). The lateral loads to the elbow were given 5 min per day for 5 weeks using 1 N force (peak-to-peak) at 5 Hz to the right arm, and left arm data was used as a contralateral control. The loading condition was determined based on our previous studies with joint loading (20, 24, 25). For the non-loading groups, sham loading was conducted in which animals were placed on the loading device but no actual loads were applied.

X-ray imaging. We conducted X-ray imaging using micro-computed tomography (Skyscan 1172 microCT scanner; Bruker-MicroCT, Kontich Belgium). The harvested bone samples were wrapped in parafilm to maintain hydration and placed in a plastic tube and oriented vertically.

Scans were performed at pixel size 6 μm. Using manufacturer-provided software and the microCT setting (26), the images were reconstructed (nRecon v1.6.9.18) and rotated (DataViewer v1.5.0). The bone mineral density (volumetric BMD) of the volume of interest (the region covering the trochlear notch, and the region distal to the trochlear notch) was measured by calculating the mean attenuation coefficient after calibration using two hydroxyapatite phantoms with 0.25 and 0.75 g/cm^3 densities. We also determined BV/TV, in which BV = bone volume, and TV = total volume.

Histology. Histology was conducted using the procedure previously described (24). In brief, mice were given an intraperitoneal injection of calcein (Sigma, St. Louis, MO, USA), a fluorescent dye, at 30 μg/g body mass in weeks 3 and 4. After euthanasia, the isolated ulnae were cleaned of soft tissues, and the distal and proximal ends were cleaved to allow infiltration of the fixatives with 10% neutral buffered formalin. Specimens were dehydrated in a series of graded alcohols and embedded in methyl methacrylate (Aldrich Chemical Co., Milwaukee, WI, USA). The transverse sections were removed from the proximal ulna, ~5 mm distant from the proximal end and mounted on a slide.

Finite element (FE) analysis. FE analysis was conducted using ANSYS workbench 17.1 (ANSYS, Canonsburg, PA, USA) for a mouse ulna sample. Using microCT images, the proximal ulna was segmented and meshed with MIMICS 16 (Materialise, Leuben, Belgium) using the procedure previously described (27). The proximal ulna was meshed into ~110,000 tetrahedral elements. A lateral load of 1 N was applied to the proximal end of the ulna (elbow loading). The deformations and stresses resulting from the applied loads were computed. In this

analysis, we employed Young's modulus of 8.9 GPa and Poisson's ratio of 0.35 for bone (27, 28), and 0.5 MPa and 0.45 for soft tissue considering material properties of the skin and muscle of rodents (29-31). We employed three loading and boundary conditions in response to elbow loading with 1-N loads: lateral loads applied at two opposing locations; lateral loads applied at a single site on one side and three supporting sites on the other side; and lateral loads on a pair of soft disks that sandwiched the elbow.

Statistical consideration. Statistical significance among groups was examined using one-way analysis of variance, and *post hoc* tests were conducted using Fisher's protected least significant difference for pairwise comparisons. Statistical significance was assumed at $p < 0.05$. The single, double, and triple asterisks indicate $p < 0.05$, $p < 0.01$, and $p < 0.001$, respectively.

Results

Elbow loading and its effect on BMD on the proximal ulna

Using μCT images, we first examined whether the proximal ulna is sensitive to ovariectomy surgery, which is considered to mimic postmenopausal osteoporosis, and thus present reduction in BMD (**Fig. 1C**). In the trochlear notch region in the proximal ulna (**Fig. 2A**), our X-ray measurement showed that OVX mice had significantly reduced BMD ($p < 0.001$; N = 10) (**Fig. 2B**). We next examined whether elbow loading contributed to prevention of OVX-induced reduction in BMD. Interestingly, the result revealed that regardless of ovariectomy, the loaded groups presented larger BMD than the non-loaded groups (**Fig. 2C**). Furthermore, in the comparison of right (loaded) vs. left (non-loaded) ulnae in the same group, loaded limbs showed higher BMD than non-loaded limbs (**Fig. 2D**). The observed reduction in BMD by ovariectomy as well as its elevation by elbow loading was also evident in the distal olecranon region - the zone of the proximal ulna that includes the cortical bone region ~1 mm distal to the trochlear notch (**Fig. 3**). Besides BMD in μCT images, bone volume (BV) was also reduced in the OVX mice (**Fig. 4A**) and increased by elbow loading (**Fig. 4B**). We further examined BMD at two circular regions (**1** and **2**), which were in contact with the applied load. The result showed that BMD in region **2** was marginally but statistically significantly greater in loaded limbs than non-loaded limbs ($p = 0.02$, N = 5; **Fig. 4C**).

Strain distribution in response to 1 N loads with elbow loading

Animal experiments clearly showed that elbow loading is capable of elevating BMD in the proximal ulna. Since load-induced strain in bone is one of the factors considered to contribute to bone formation, we next conducted FE analysis and estimated strain distributions in the proximal

tibia. In the first FE analysis, a pair of 1 N lateral forces were applied at two opposing locations (**Fig. 5A&B**). We focused on the minimum principal elastic strain (3rd principal strain), which is compressive. In the medial and lateral surfaces, the regions with strain larger than 0.1% (boundary between the green and cyan labels) are concentrated in the area within ~0.5 mm from the loaded site. In the cross-section, the maximum strain appeared on the periosteal surface at the loading site. In the second FE analysis, 1 N loads were applied at a single site on one side and three supporting sites on the other side (**Fig. 5C&D**). Similar to the results in the first analysis, strains exceeding 0.1% (1,000 μstrain) are confined to the vicinity of the loading site and supporting points. Compared to strain at the single loading site, three supporting sites significantly reduced the maximum compressive strain by ~10-fold (from ~ 2% in the dark blue label to ~ 0.1% in the cyan level).

Compression of the proximal ulna by soft tissue.

During *in vivo* loading, surrounding tissues are expected to further lower the maximum strain value. To evaluate indirect loading to the ulna via soft surrounding tissue, we conducted a third FE analysis in which the ulna was sandwiched between a pair of softer disks (0.5 MPa with Poison ratio of 0.45; 9 mm in diameter) (**Fig. 6A**). Of note, Young's modulus of bone is assumed to be 8.9 GPa with Poison ratio of 0.35 in all FE models. Application of 1 N loads onto the top disk of soft tissue generates strain in soft disks. Compression of a pair of soft tissue disks induced multiple strain spots that were widely distributed from the proximal tip to the whole elbow joint (**Fig. 6B**). The result showed that the maximum strain was significantly smaller than 0.1% (boundary between the green and cyan indicators) in the trochlear notch and surrounding region, except for the loading site on the periosteal surface. The high strain, ~0.05 to 0.1%,

appeared mostly on the restricted surface of the cross-sections, which are indicated with the arrow (**Fig. 6C**).

Evaluation of the predicted strain on the proximal cross-sections.

To evaluate any linkage of the predicted strain distribution with load-driven bone formation, we conducted histological analysis using calcein-labeled cross-sections of the proximal ulna distal to the trochlear notch. Of note, calcein uptake marked newly formed bone on the endosteal and periosteal surfaces. The result revealed that OVX mice consistently presented less label in the endosteal surface than the sham OVX mice (**Fig. 7A&B**). In both sham OVX and OVX mice, the result also showed that elbow loading induced more calcein label on the periosteal surface than the endosteal surface. This observation indicates that the periosteal surface is more sensitive to elbow loading than the endosteal surface, possibly because of larger strain values on the periosteal surface than the endosteal surface (**Fig. 6C**). Focusing on two specific regions (**a** and **b** in **Fig. 7C**) that presented high compressive strains on the periosteal surface, we determined the length of the calcium-labeled surface with and without elbow loading in sham OVX mice. We defined two regions, **a** and **b**, with 4 orthogonal lines, in which two lines defined the edge of the bone cavity and two other lines defined the lower portion of ulnar cortical bone. The result showed that calcein label lengths in these two regions were significantly greater for the loaded group than the non-loaded group (N = 5; $p = 0.04$ and 0.007 for regions **a** and **b**, respectively) (**Fig. 7D**).

Discussion

Elbow loading generates artificial lateral forces that are rarely encountered during routine physical activity. Unlike axial or bending loads with ulna loading or tibia loading, the mechanical response of synovial joints, such as the elbow, to lateral loads has not been fully characterized. Using two mouse models (normal and postmenopausal osteoporosis), we applied daily loads of 1 N at 5 Hz for 5 min to the left elbow and found that this dynamic loading modality is able to increase volumetric BMD in the proximal ulna. Of note, ulna loading is commonly used to stimulate bone formation in mouse ulnae, and FE analysis using ~16-week old C57BL/6 mice reported ~1,750 μstrain as a minimum effective strain value in response to loads at 0.5 to 3.1 N (32). While this study employed ~12-week BALB/c mice with 1 N loads, the predicted strain value varied in a complex geometry in the elbow with three boundary conditions in FE analysis. When the soft surrounding tissue is modeled in the third analysis, a widely distributed strain was observed in the trochlear notch and surrounding area, in which the compression strain value was mostly in the yellow zone with < 1,000 μstrain.

In our animal experiment with 4 groups (sham OVX and OVX mice with and without elbow loading), ovariectomy surgery reduced BMD by 6% (trochlear notch) and 5% (distal olecranon including cortical bone ~1 mm distal to the trochlear notch) in the proximal ulna. Furthermore, elbow loading elevated BMD by 3 to 4% in sham OVX mice and 6 to 8% in OVX mice in two separate comparisons: one comparison between the loaded group and non-loaded group, and the other comparison between the loaded right and non-loaded left limbs. In both comparisons, OVX mice appeared to be more sensitive to elbow loading than sham OVX mice. The bone's mechanical sensitivity differs depending on genetic backgrounds and ages, and further

quantitative analysis is required to determine efficiency of stimulatory loading effects in control and osteoporotic animals (33). Besides volumetric BMD, bone volume was reduced by ovariectomy surgery and increased by elbow loading both in the OVX and sham OVX groups.

In response to lateral loads of 1 N to the elbow, this study predicted the distribution of minimum principal elastic strain (the third principal strain) and compressive strain. Our primary focus was detecting regions that presented 1,000 μstrain or more, since pre-clinical data indicate that load-driven bone formation may require a threshold strain value, minimum effective strain, above 1,000 μstrain (34). The minimum effective strain is considered to be a boundary value that separates resorption-dominant and formation-dominant bone remodeling. While this value is reported to be ~1,000 μstrain in pre-clinical studies with avian ulna, rat tibia, and mouse tibia, the value differs depending on the loaded sites (35).

In the first and second FE analyses with 1 N at the lateral and medial sides, strain larger than 1,000 μstrain was concentrated in the zone within ~0.5 mm of the plane that included the applied forces. In the third FE analysis in which the proximal ulna was sandwiched between a pair of soft tissue disks, the overall strain values were significantly smaller than those in the first and second tests. The maximum compressive strain in the first and second tests was 7.2% and 2.1%, respectively, while that in the third test with soft tissues was 0.67%. These maximum values were the result of stress concentrations, and exact values heavily depend on the mechanical properties of surrounding tissues. They may potentially damage loaded bone, although no obvious bone defects were detectable in X-ray imaging of harvested bone samples. The prediction in the third test with soft surrounding tissue is expected to be closer to *in vivo*

responses than those in the first and second tests. Analysis of calcein staining in the regions of maximum strain induced by elbow loading found that those regions underwent additional bone formation in the loaded mice. This result suggests that the FE model's prediction of regions of high strain correlates with the observed regions of increased bone formation.

There are limitations in this study. While our FE analysis was focused on one representative bone sample, there are variations in stiffness among animals. These variations can be affected not only by efficacy of elbow loading but also size and geometry of individual samples. Of note, the overall weight of animals was approximately 6% higher in OVX mice than sham OVX mice. The minimum effective strain value is reported to be dependent on loading frequency, and further analysis is needed to evaluate frequency dependence (36, 37). We observed a tendency of large strain values on the calcein-stained periosteal surface, and the regions of higher model-predicted strain showed more calcein staining in loaded groups. Further quantitative approaches are necessary to establish the relationship between these high strain regions and bone formation.

In summary, this study shows that elbow loading with 1 N force is predicted to induce compressive strain of < 1,000 μstrain in the trochlear notch and surrounding area, except for the restricted periosteal surface near the loading site. We found that BMD is elevated in cortical bone with less than 1,000 μstrain, and calcein staining is increased in bone regions with higher predicted strain. Future structural characterization in response to elbow loading may contribute to understanding of the mechanism of load-driven bone formation and suppression of tissue inflammation.

Acknowledgements

This study was in part supported by the funds from NIH R01 AR052144 (HY), AR053237 (AGR), and Osaka University Scholarship for Overseas Research Activities (RK).

Author contributions

Conception and experimental design: FJ, AJ, CD, AC, SL, KM, TH, BL, AR, JC, and HY

Data collection and interpretation: FJ, AJ, CD, SL, RK, and KM

Drafted manuscript: FJ, AC, AR, JC, and HY

References

1. Taylor AH, Cable NT, Faulkner G, Hillsdon M, Narici M, Van Der Bij AK (2004). Physical activity and older adults: a review of health benefits and the effectiveness of interventions. J Sports Sci 22:703–25.
2. Fuchs RK, Shea M, Durski SL, Winters-Stone KM, Widrick J, Snow CM (2007). Individual and combined effects of exercise and alendronate on bone mass and strength in ovariectomized rats. Bone 41:290–6.
3. Turner CH, Robling AG (2005). Mechanisms by which exercise improves bone strength. J Bone Miner Metab 23:16–22.
4. Burr DB, Robling AG, Turner CH. (2002). Effects of biomechanical stress on bones in animals [review]. Bone 30:781–6.
5. Bonewald LF (2006). Mechanosensation and transduction in osteocytes. Bonekey 3:7-15.
6. Robling AG (2013). The expanding role of Wnt signaling in bone metabolism. Bone 55:256-257.
7. Robling AG, Turner CH (2009). Mechanical signaling for bone modeling and remodeling. Crit Rev Eukaryot Gene Expr 19:319-338.
8. Silva MJ, Brodt MD, Lynch MA, Stephens AL, Wood DJ, Civitelli R (2012). Tibia loading increases osteogenic gene expression and cortical bone volume in mature and middle aged mice. PLoS One 7:e34980.
9. Dodge, T., Wanis, M., Ayoub, R., Zhao, L., Watts, N.B., Bhattacharya, A., Akkus, O., Robling, A., Yokota, H. (2012). Mechanical loading, damping, and load-driven bone formation in mouse tibiae. *Bone* 51:810-818.
10. Robling AG, Castillo AB, Turner CH (2006). Biomechanical and molecular regulation of bone remodeling. Ann Rev Biomed Eng 8:455-498.
11. Burger EH, Klein-Nulend J (1999). Mechanotransduction in bone – role of the lacuno canalicular network. FASEB J 13:S101-102.
12. Zhang P, Malacinski GM, Yokota H (2008). Joint loading modality: its application to bone formation and fracture healing. Br. J. Sports Med. 42:556-560.
13. Zhang, P., Turner, C.H., Yokota, H. (2009). Joint loading-driven bone formation and signaling pathways predicted from genome-wide expression profiles. *Bone* 44:989-998.
14. Zhang, P., Hamamura, K., Yokota, H., Malacinski, G.M. (2008). Potential applications of pulsating joint loading in sports medicine. *Exercise Sports Med. Rev.* 37:52-56.
15. Hamamura, K., Zhang, P., Zhao, L., Shim, J.W., Chen, A., Dodge, T.R., Wan, Q., Shih, H., Na, S., Lin, C.C., Sun, H.B., Yokota, H. (2013). Knee loading reduces MMP13 activity in the mouse cartilage. *BMC Musculoskeletal Disorders* 14:312.
16. Yokota, H., Leong, D.J., Sun, H.B. (2011). Mechanical loading: bone remodeling and cartilage maintenance. *Current Osteoporosis Res.* 9:237-242.
17. Zhang, P., Sun, Q., Turner, C.H., and Yokota, H. (2007). Knee Loading Accelerates Bone Healing in Mice. *J. Bone Miner. Res*. 22:1979-1987.
18. Zhang, P., Yokota, H. (2011). Knee loading stimulates healing of mouse bone wound in a femur neck. *Bone* 49:867-872.
19. Sun, H., Zhao, L., Tanaka, S., Yokota, H. (2011). Moderate joint loading reduces degenerative actions of matrix metalloproteinases in the articular cartilage of mouse ulnae. *Connective Tissue Res.* 53:180-186.

20. Zhang, P., Yokota, H. (2012). Elbow loading promotes longitudinal bone growth of the ulna and the humerus. *J. Bone Miner. Metab*. 30:31-39.
21. Liu D, Zhang Y, Li X, Li J, Yang S, Xing X, Fan G, Yokota H, Zhang P (2017). eIF2α signaling regulates ischemic osteonecrosis through endoplasmic reticulum stress. *Scientific Reports* 7:5062.
22. Li, X, Yang, J., Liu, D., Li, J., Niu, K., Feng, S., Yokota, H., Zhang, P. (2016). Knee loading inhibits osteoclast lineage in a mouse model of osteoarthritis. *Scientific Reports* 6:24668.
23. Tan N, Li X, Zhai L, Liu D, Li J, Yokota H, Zhang P (2018). Effects of knee loading on obesity related nonalcoholic fatty liver disease in an ovariectomized mouse model with high fat diet. *Hepatology Res*. doi:10.1111/hepr.13076.
24. Yokota, H., and Tanaka, S.M. (2005). Osteogenic potentials with joint loading modality. *J. Bone Mineral Metabolism* 23:302-308.
25. Zhang, P., Tanaka, S.M., Sun, Q., Turner, C.H., and Yokota, H. (2007). Frequency-dependent enhancement of bone formation in murine tibiae and femora with knee loading. *J. Bone Miner. Metabolism* 25:383-391.
26. Bouxsein ML, Boyd SK, Christiansen BA, Guldberg RE, Jepsen KJ, Muller R (2010). Guidelines for assessment of bone microstructure in rodents using micro-computed tomography. *J Bone Miner Res* 25:1468-1486.
27. Jiang F, Liu S, Chen A, Li B-Y, Robling AG, Chen J, Yokota H (2018). Finite element analysis of the mouse distal femur with tumor burden in response to knee loading. *International J Orthopaedics* 5:1-9.
28. Chattah NL, Sharir A, Weiner S, Shahar R (2009). Determining the elastic modulus of mouse cortical bone using electronic speckle pattern interferometry and micro computed tomography: a new approach for characterizing small-bone material properties. *Bone* 45:84-90.
29. Wei J, Crichton M, Kendall M (2016). Measuring key skin mechanical properties of different animal models to facilitate medical device translation. *Proc. 22nd Congress of the Euro Soc Biomechanics*. Lyon, France.
30. Ogneva IV, Lebedev DV, Shenkman BS (2010). Transversal stiffness and Young's modulus of single fibers from rat soleus muscle probed by atomic force microscopy. *Biophys J* 98:418-424.
31. Karimi A, Rahmati SM, Navidbakhsh M (2015). Mechanical characterization of the rat and mice skin tissues using histostructural and uniaxial data. *Bioengineered* 6:153-160.
32. Norman SC, Wagner DW, Beaupre GS, Castillo AB (2015). Comparision of three methodsof calculating strain in the mouse ulna in exogenous loading studies. J. Biomechanics 48:53-58/
33. Bergmann P, Body JJ, Boonen S, Boutsen Y, Devogelaer JP, Goemaere S, Jaufman J, Reginster JY, Rozenberg S (2011). Loading and skeletal development and maintenance. J. Osteoporosis 2011: ID786752.
34. Hsieh YF, Robling AG, Ambrosius WT, Burr DB, Turner CH (2001). Mechanical loading of diaphyseal bone in vivo: the strain threshold for an osteogenic response varies with location. *J. Bone Miner. Res.* 16:2291-7.
35. Sugiyama T, Meakin LB, Browne WJ, Galea GL, Price JS, Lanyon LE (2012). Bones' adaptive response to mechanical loading is essentially linear between the low strains associated with disuse and the high strains associated with the lamellar/woven bone transition. *J. Bone Miner. Res.* 27:1784-1793.

36. Xie L, Jacobson JM, Choi ES, Busa B, Donahue LR, Miller LM, Rubin CT, Judex S (2006). Low level mechanical vibrations can influence bone resorption and bone formation in the growing skeleton. *Bone* 39:1059-1066.
37. Sugiyama T, Meakin LB, Browne WJ, Galea GL, Price JS, Lanyon LE (2012). Bones' adaptive response to mechanical loading is essentially linear between the low strains associated with disuse and the high strains associated with the lamellar/woven bone transition. *J. Bone Miner. Res.* 27:1784-1793.

Figure Legend

Figure 1. Elbow loading and the cross-section of the proximal ulna. (A&B) Configuration of elbow loading with the loading device. (C) μCT images of the cross-sections of the proximal ulna, ~ 1 mm distal to the edge of the trochlear notch.

Figure 2. Loading effect on BMD in the trochlear notch. The single and triple asterisks indicate $p < 0.01$ and $p < 0.001$, respectively. (A) Proximal ulna, covering the trochlear notch. (B) Reduction in BMD by ovariectomy surgery. (C) Increase in BMD in the loaded group compared to the non-loaded group. (D) Increase in BMD in the loaded limb compared to the non-loaded limb.

Figure 3. Loading effect on BMD in the distal olecranon. The single, double, and triple asterisks indicate $p < 0.05$, $p < 0.01$ and $p < 0.001$, respectively. (A) Distal olecranon including ~ 1 mm distal to the edge of the trochlear notch. (B) Reduction in BMD by ovariectomy surgery. (C) Increase in BMD in the loaded group compared to the non-loaded group. (D) Increase in BMD in the loaded limb compared to the non-loaded limb.

Figure 4. Loading effect on bone volume. The single and triple asterisks indicate $p < 0.01$ and $p < 0.001$, respectively. (A) Reduction in bone volume (BV), normalized by total volume (TV), by ovariectomy surgery. (B) Increase in BV/TV in the loaded group compared to the non-loaded group. (C) BMD at two circular regions (**1** and **2**; 100 μm in diameter) in the distal olecranon (0.75 mm in length) with and without elbow loading in sham OVX mice.

Figure. 5. Strain distribution in response to 1 N lateral forces. (A) Meshing of the proximal ulna with two loading sites with the red arrows. (B) Minimum principal strain distribution on the surface and cross-section of the proximal ulna with a single point support. Strain larger than 0.1% (boundary between the green and cyan labels) is concentrated in the area within 0.5 mm from the loaded site. (C) Loading configuration with a three-point support. (D) Minimum principal strain distribution on the side of 1 N application (plane x) and on the other side with three supporting points (plane y) with a three-point support.

Figure. 6. Compression of the proximal ulna with a pair of soft tissues. (A) Configuration of the ulna, sandwiched by a pair of soft disks. The top disk moves downward (plane x), while the bottom disk is stationary (plane y). (B) Minimum principal strain distribution on the proximal ulna by compression with a pair of soft tissue disks. The compressive strain in the distal to the trochlear notch is significantly smaller than 0.1% (boundary between sky blue and navy blue indicators). (C) Minimum principal strain distribution of the cross-sections, 1, 1.5, 1.75, and 2 mm distal to the proximal edge of the trochlear notch. The arrow indicates the region with high strain.

Figure 7. Calcein-stained cross-sections of the proximal ulna distal to the trochlear notch. (A) Sections from sham OVX mice with and without elbow loading. (B) Sections from OVX mice with and without elbow loading. (C&D) Calcein-stained length in the regions, **a** and **b**, with and without elbow loading for sham OVX mice. Two regions were defined with 4 orthogonal lines. Of note, length of the double-stained surface was multiplied by two.

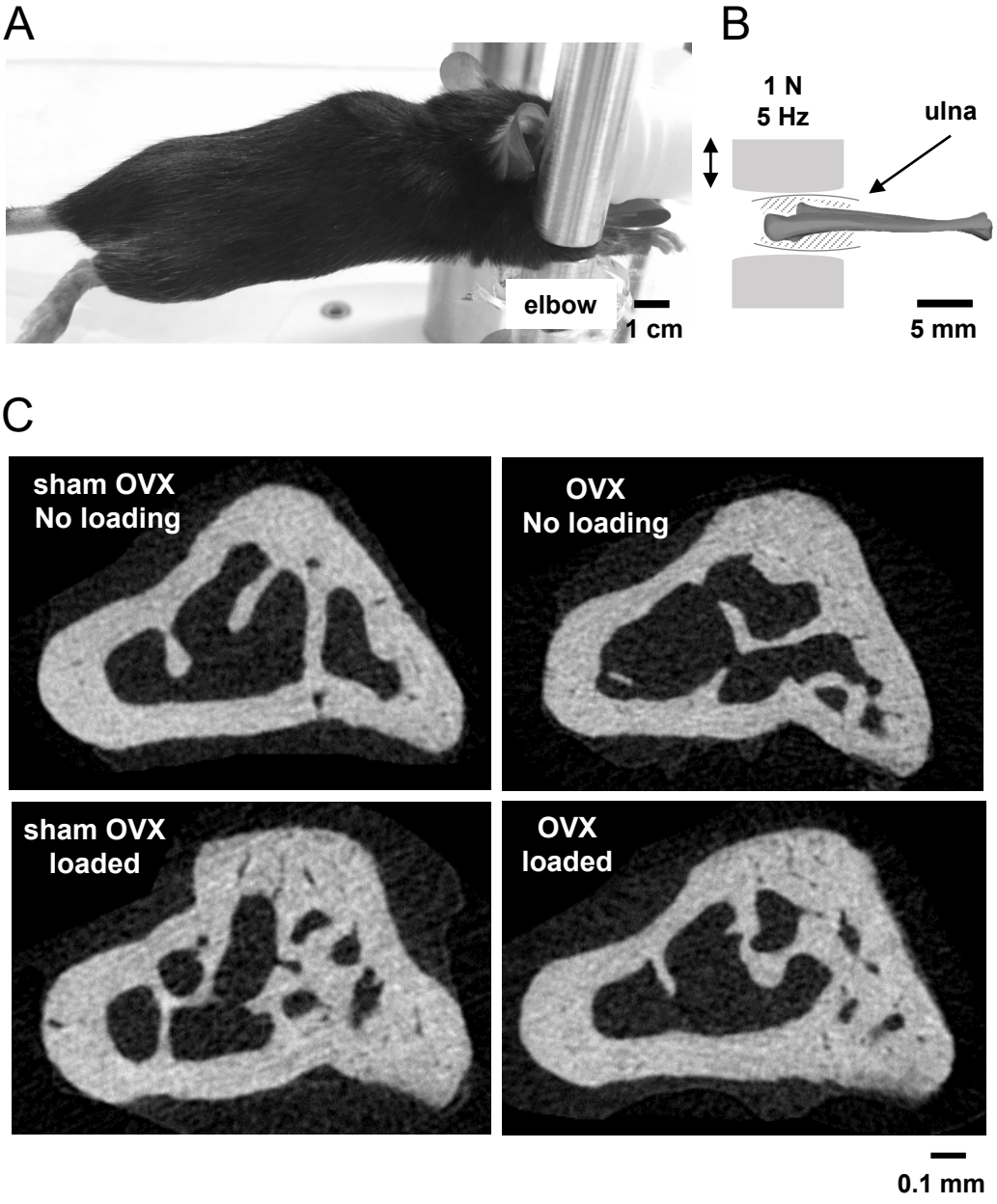
A
elbow
1 cm
B
1 N
5 Hz
ulna
5 mm
C
sham OVX
No loading
OVX
No loading
sham OVX
loaded
OVX
loaded
0.1 mm

Figure 1

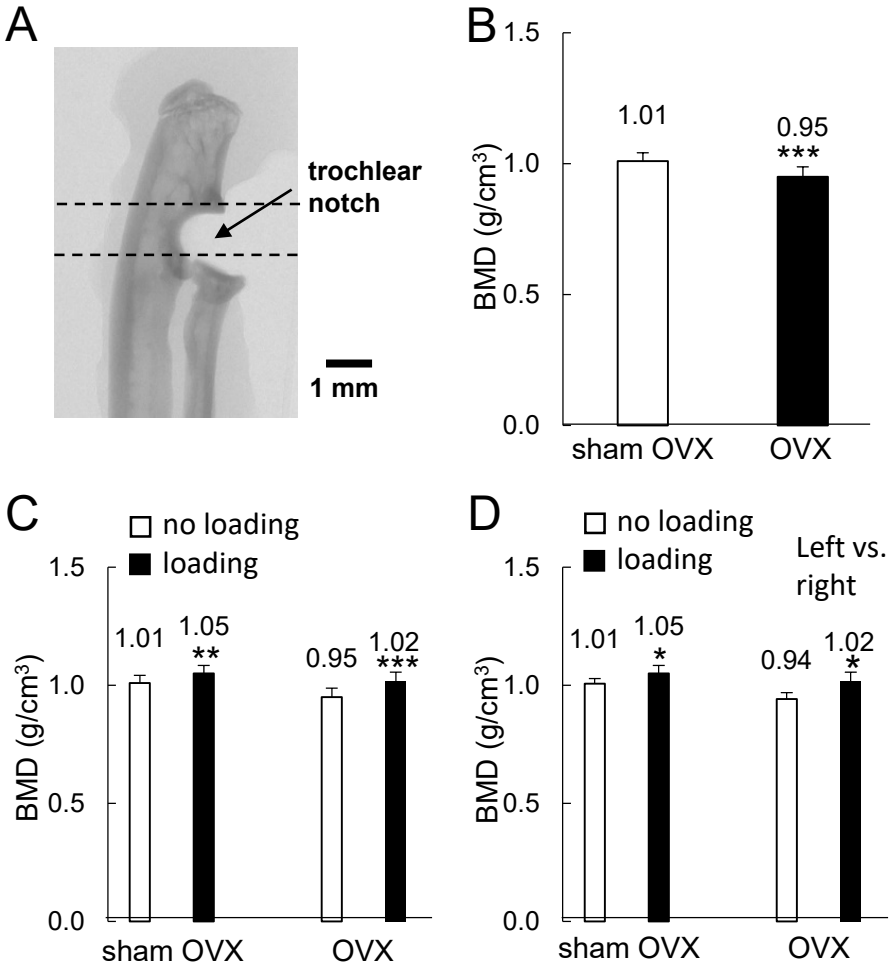
A
trochlear notch
1 mm
B
BMD (g/cm3)
1.5
1.0
0.5
0.0
1.01
0.95
***
sham OVX
OVX
C
no loading
loading
1.01
1.05
**
0.95
1.02
***
sham OVX
OVX
D
no loading
loading
Left vs. right
1.01
1.05
*
0.94
1.02
*
sham OVX
OVX

Figure 2

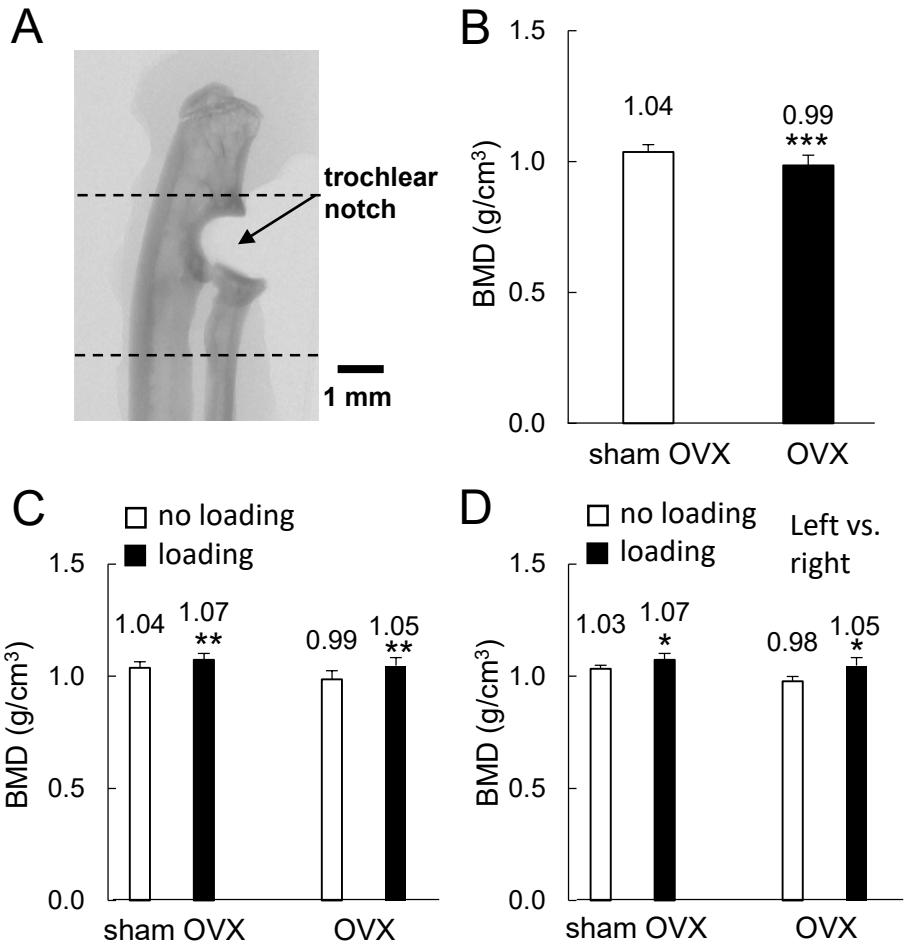
A
trochlear notch
1 mm
B
BMD (g/cm3)
1.5
1.0
0.5
0.0
1.04
0.99
***
sham OVX
OVX
C
no loading
loading
1.04
1.07
**
0.99
1.05
**
sham OVX
OVX
D
no loading
loading
Left vs. right
1.03
1.07
*
0.98
1.05
*
sham OVX
OVX

Figure 3

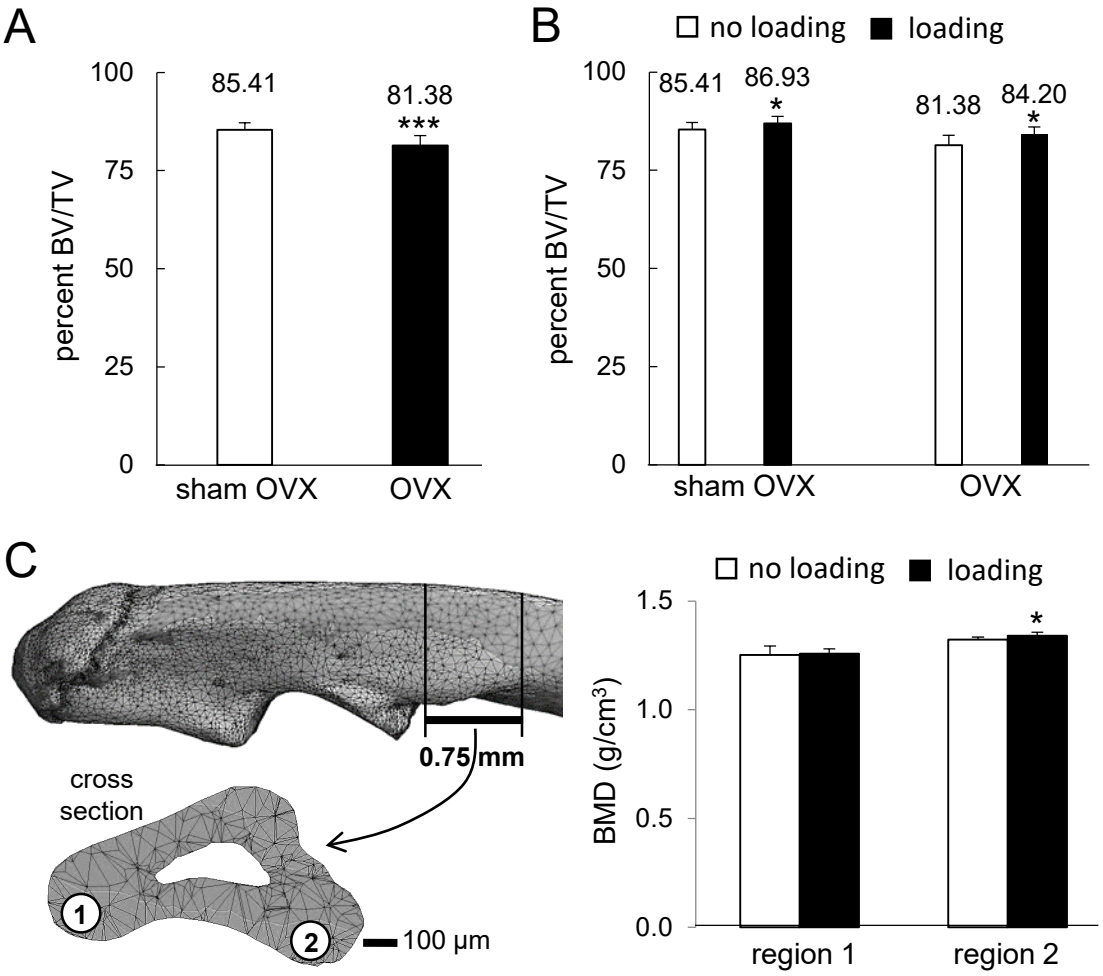
A
100
75
50
25
0
percent BV/TV
85.41
81.38
***
sham OVX
OVX
B
no loading
loading
85.41
86.93
*
81.38
84.20
*
sham OVX
OVX
C
0.75 mm
cross section
1
2
100 µm
no loading
loading
1.5
1.0
0.5
0.0
BMD (g/cm³)
*
region 1
region 2

Figure 4

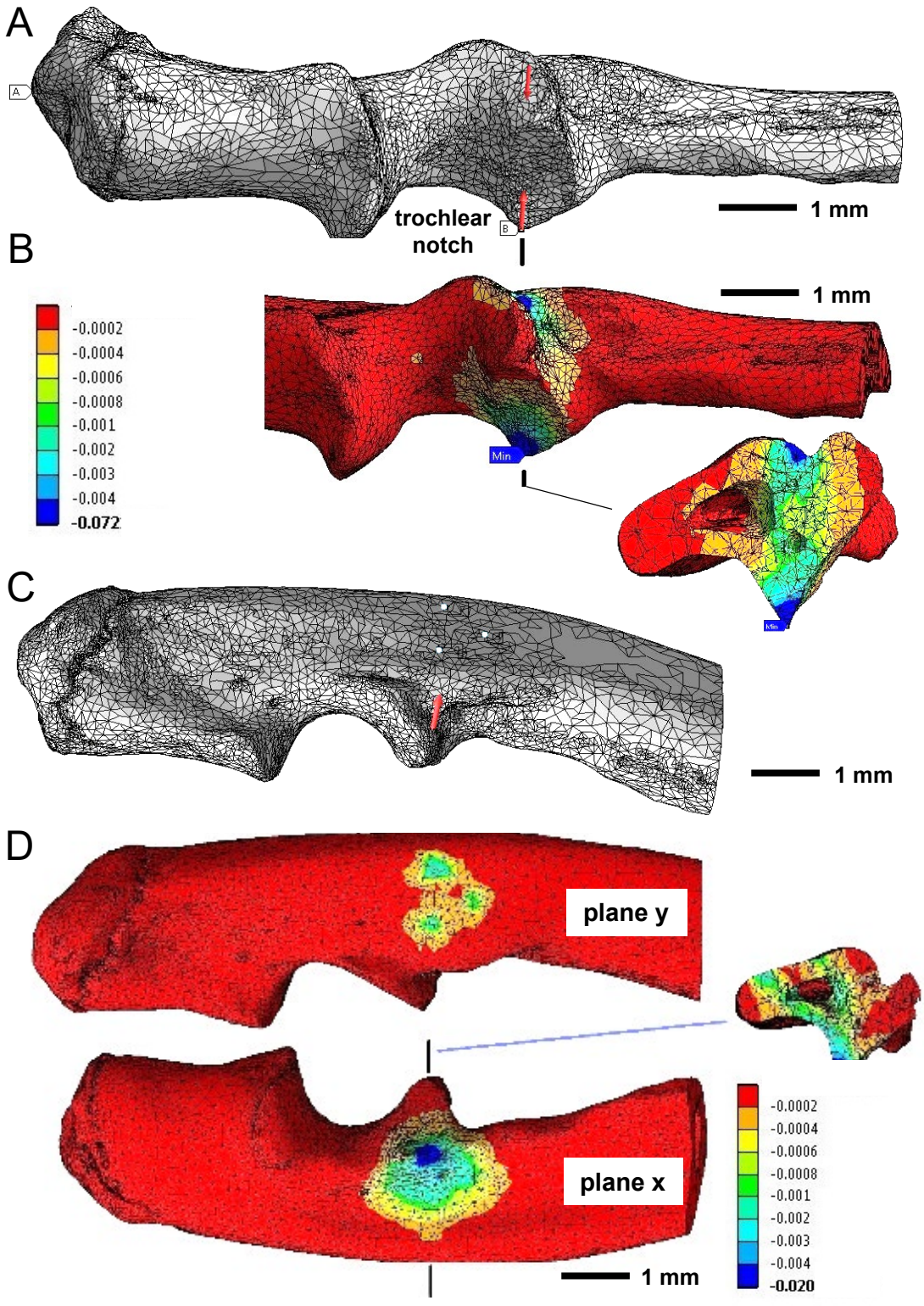
A
trochlear notch
1 mm
B
-0.0002
-0.0004
-0.0006
-0.0008
-0.001
-0.002
-0.003
-0.004
-0.072
1 mm
C
1 mm
D
plane y
plane x
1 mm
-0.0002
-0.0004
-0.0006
-0.0008
-0.001
-0.002
-0.003
-0.004
-0.020

Figure 5

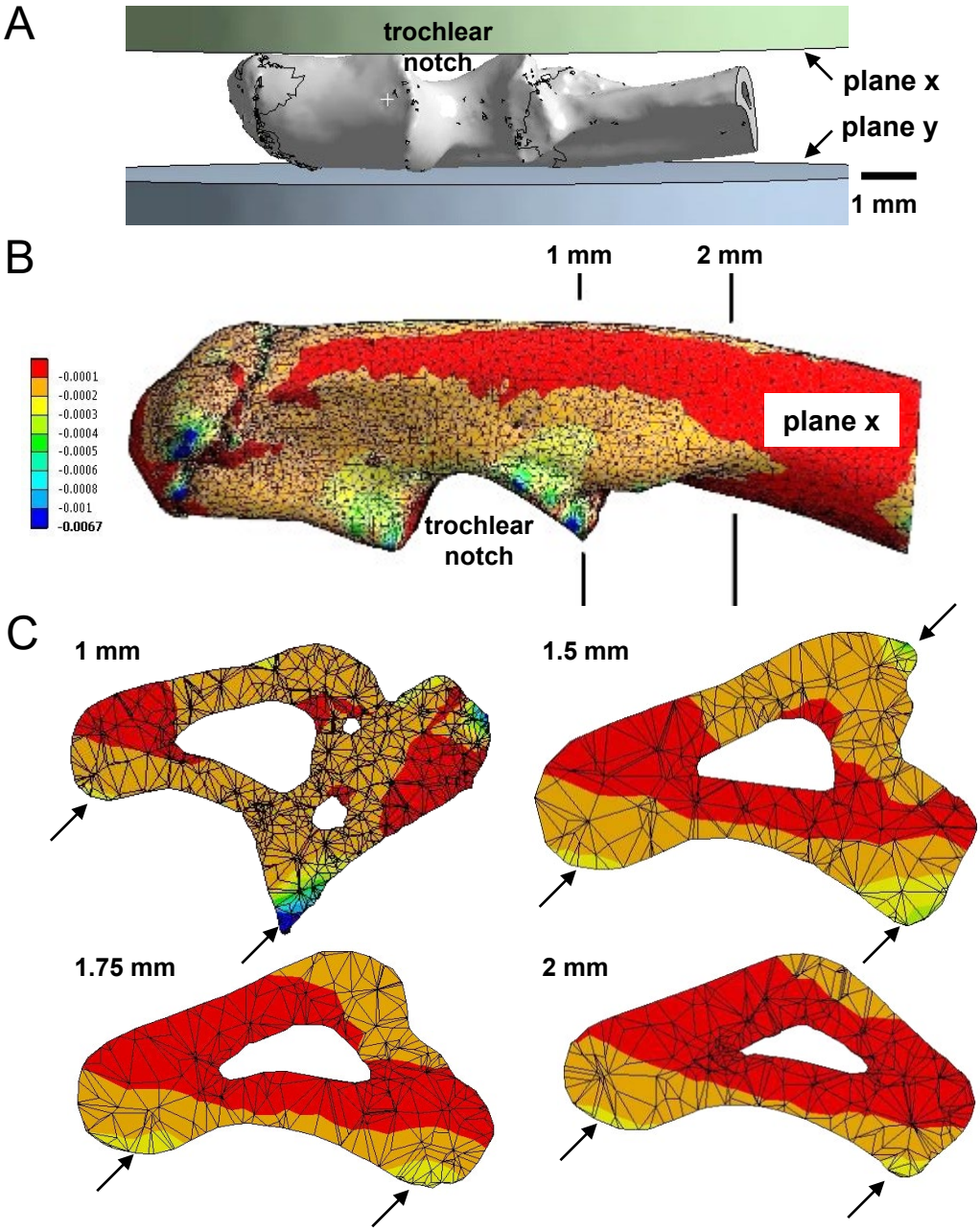
A
trochlear notch
plane x
plane y
1 mm
B
1 mm
2 mm
-0.0001
-0.0002
-0.0003
-0.0004
-0.0005
-0.0006
-0.0008
-0.001
-0.0067
plane x
trochlear notch
C
1 mm
1.5 mm
1.75 mm
2 mm

Figure 6

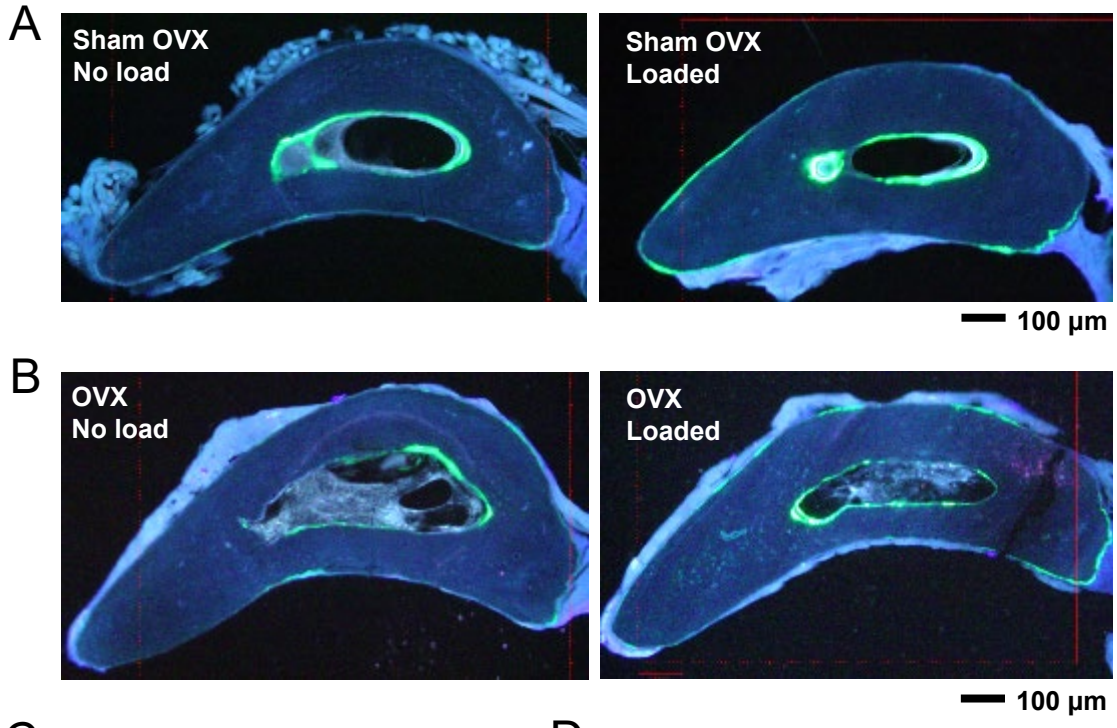
A
Sham OVX
No load
Sham OVX
Loaded
100 μm
B
OVX
No load
OVX
Loaded
100 μm
C
low strain
region
a
high strain region
b
D
calcein-stained length
(mm)
0.5
0.4
0.3
0.2
0.1
0
*
***
no loading
loading
region a
region b

Figure 7